AD-A093 970 ARMY RESEARCH AND TECHNOLOGY LABS MOFFETT FIELD CA A--ETC F/G 20/4
VISCOUS-INVISCID INTERACTION ON OSCILLATING AIRFOILS IN SUBSONI--ETC(U)
JAN 81 W J MCCROSKEY, S L PUCCI

UNCLASSIFIED NL

END
DATE FILMED
2 81
DTIC

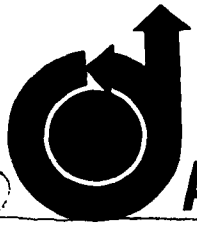

# AIAA-81-0051
# Viscous-Inviscid Interaction on Oscillating Airfoils

W.J. McCroskey and S.L. Pucci,
U.S. Army Aeromechanics Laboratory,
(AVRADCOM),
Ames Research Center, NASA
Moffett Field, CA.



**AIAA 19th AEROSPACE SCIENCES MEETING**

January 12-15, 1981/St. Louis, Missouri

# VISCOUS-INVISCID INTERACTION ON OSCILLATING AIRFOILS IN SUBSONIC FLOW

W. J. McCroskey* and S. L. Pucci†
U.S. Army Aeromechanics Laboratory (AVRADCOM)
Ames Research Center, Moffett Field, California

## Abstract

Selected results from an extensive oscillating-airfoil experiment are analyzed and reviewed. Four distinct regimes of viscous-inviscid interaction are identified, corresponding to varying degrees of unsteady flow separation. The dominant fluid dynamic phenomena are described for each regime. Ten specific test cases, including the appropriate flow conditions and experimental results, are proposed for evaluating unsteady viscous theories and computational methods.

## I. Introduction

Important viscous phenomena combine with unsteady effects in a variety of current aeronautical, hydrodynamic, and wind-energy problems. Consequently, several recent investigations have attempted to predict, compute, or empirically correlate the unsteady airloads on oscillating airfoils that experience varying degrees of flow separation, and additional work is in progress at a number of research centers. The results are mixed, and conflicting claims abound; this is partly because the difficulty of the problem increases rapidly with increasing amounts of separation, and partly because definitive data over wide ranges of separated flow conditions do not exist.

The authors and their colleagues have recently concluded an extensive experimental investigation of boundary-layer transition, separation, and unsteady stall on oscillating airfoils in two-dimensional subsonic flow. The experiment included more than 50 combinations of $M_\infty$ and parameters of the unsteady motion for each of eight different airfoil sections. Highlights of the principal results, insofar as the extensive lift, drag, and pitching moment data are concerned, were described recently in Ref. 1. The purpose of the present paper is to extract from a limited number of these test points, the specific details and experimental information that might serve to guide the development of new unsteady viscous theories and computational methods. A hierarchy of model problems can be developed, corresponding to increasing amounts of interaction between the viscous and inviscid parts of the flow field. Within each level, specific sets of data are proposed that can be used as test cases for evaluating existing and future prediction methods.

The data for the present paper were obtained from the three airfoils shown in Fig. 1. Pressure and hot-wire instrumented models, 0.62-m chord and 2.1-m span, were oscillated in pitch, $\alpha = \alpha_0 + \alpha_1 \sin \omega t$, about an axis at $x/c = 0.25$ in a 2.1- by 3.0-m atmospheric-pressure, solid-wall wind tunnel. The effects of the tunnel walls are thought to be small, but not negligible.

The free-stream Mach number was varied between 0.07 and 0.30, with important consequencies;[1] however, only the data at $M_\infty = 0.30$ are presented here. For this Mach number, the Reynolds number was approximately $4 \times 10^6$ based on chord, and the reduced frequency parameter, $k = \omega c/2U_\infty$, varied from 0 to 0.20.

Details of the instrumentation, experimental procedures, measurement uncertainties, and test conditions, as well as the coordinates of each airfoil, are documented in Ref. 2. That reference also describes the computer data tapes, which will be made available upon request.

## II. Summary of the Viscous-Inviscid Interaction Regimes

The overall features of the flow field around an airfoil in subsonic flow are primarily characterized by the degree or extent of flow separation. For a given airfoil, the primary parameter that determines the degree of separation is the maximum angle of attack ($\alpha_{max} = \alpha_0 + \alpha_1$ for sinusoidal oscillations). An important aspect of the flows discussed in this paper is the large amplitudes, $\alpha_1$, that produce the large maximum angles. This contrasts with the hierarchy of viscous effects on oscillating airfoils at transonic speeds and low angles of attack,[3,4] where the scale of the interaction is governed primarily by the strength and motion of the shock wave. So far, prediction methods for this class of problems have not been successful for the low-speed, high-angle problems, and vice versa.

The importance of $\alpha_{max}$ is illustrated in Fig. 2, which portrays four important regimes of viscous-inviscid interaction for oscillating airfoils. For the left-hand part of the figure, that is, $\alpha_{max} = 13°$, there was almost no separation throughout the cycle, although unsteady boundary-layer displacement thickness effects were not completely negligible. When $\alpha_{max}$ was increased to 14°, the limited separation that occurred during a small fraction of the cycle distorted the hysteresis loops of the unsteady pressures and airloads. From a practical standpoint, the effect on $C_M$ is particularly important. This stall-onset condition represents the limiting case of the maximum lift that can be obtained with no significant penalty in pitching moment or drag.

A slight additional increase in $\alpha_{max}$ to 15° produced a major increase in the extent, severity, and duration of the separation phenomenon, for the conditions shown in Fig. 2. This type of viscous-inviscid interaction produced what is called light dynamic stall.[1] Further increases in $\alpha_{max}$ led to the deep dynamic stall regime, with a large viscous zone over the entire upper surface of the airfoil during half or more of the cycle.

Within each of the stall regimes shown in Fig. 2, the details of the flow field depend on Mach number, Reynolds number, airfoil shape, and the

*Senior Staff Scientist, NASA Thermo- and Gas-Dynamics Division. Associate Fellow AIAA.
†Research Engineer. Member AIAA.

airfoil motion, $\alpha(t)$. To a first approximation, $M_\infty$ and leading-edge geometry are the principal determinants of the type of boundary-layer separation (for example, leading-edge, trailing-edge, or mixed separation characteristics), although changes from one type to another can occur as the frequency of the oscillation increases.[1] For a given class of separation or stall behavior, the amplitude $\alpha_1$ and reduced frequency $k = \omega c/2U_\infty$ largely determine the stall and reattachment angles and the size and shape of the hysteresis loops; or alternatively, the departure from quasi-static behavior.

More detailed descriptions of the various stall mechanisms can be found in Ref. 1, Refs. 5-7, and elsewhere. However, it is apparent from the brief remarks above that passing from no stall to deep dynamic stall encompasses a wide range of viscous flow phenomena, and that realistic but efficient prediction methods should probably be tailored to the specific characteristics of the flow regime of interest. The following sections provide some specific experimental information and test cases that can be used in developing and validating new analyses and computations for each regime depicted in Fig. 2.

## III. No Stall: Weak Interactions

### General Features

If viscous effects are confined to thin boundary layers, the primary effects of oscillation can be derived from unsteady thin-airfoil theory. The first-order results for pressure and lift take the following form:

$$C_p = \mp \frac{2\alpha}{\sqrt{1 - M_\infty^2}} \sqrt{\frac{1 - x}{x}}\, f_1(x, t) \qquad (1)$$

$$C_L = \frac{2\pi\alpha}{\sqrt{1 - M_\infty^2}}\, f_2(t) \qquad (2)$$

where the minus and plus signs refer to the upper and lower surfaces, respectively. All of the unsteady effects, such as amplitude and phase changes with respect to the motion $\alpha(t)$, are contained in the functions $f_1$ and $f_2$. The remaining terms in Eqs. (1) and (2) are easily recognized as the solution for a flat plate in steady flow, and $f_1 = f_2 \to 1$ in the quasi-steady limit. The details of these unsteady solutions are readily available in the vast literature on thin-airfoil theory (e.g., Ref. 8).

A number of secondary effects, such as airfoil thickness and camber, finite mean angle of attack, large-amplitude motion, boundary-layer displacement thickness effects (including small amounts of separation), and wind-tunnel wall corrections, can be obtained, at least qualitatively, by superposition of individual corrections to the unsteady flat-plate solution. This is indicated schematically in Fig. 3 for the surface velocity, U. For quantitative precision, the pressure should be calculated from U and $\partial\phi/\partial t$, using the nonlinear Bernoulli equation. Although conceptually rather simple, accurate predictions of these effects are not trivial. Consequently, experimental test cases in this weak interaction regime represent the first level in the hierarchy of model problems to be considered. The following four examples are arranged in the order of increasing levels of complexity.

### Case 1: NACA 0012, $\alpha = 5° + 5° \sin \omega t$

Figure 4 illustrates the basic features of an oscillating airfoil with $\alpha_{max}$ rather large but well below the static stall angle. The boundary layers on both the upper and lower surfaces were fully attached throughout the cycle, except for a small separation bubble near the upper-surface leading edge for $\alpha > 5°$, which produced transition from laminar to turbulent flow.

Figure 5 shows the details of the unsteady pressure distributions by harmonic components. The $C_p$ values are plotted vs $\sqrt{x}$ rather than $x$, so as to stretch out the leading-edge region where the variations, and the discrepancies with linear theory, are the greatest. Linear theory predicts $C_{p_2} = 0$ and equal and opposite values for the individual components of $C_{p_0}$ and $C_{p_1}$ on the upper and lower surfaces, which is clearly not the case in reality. However, the general trends of the measured pressures are precisely those suggested by the linear superposition concepts indicated in Fig. 3, provided the nonlinear Bernoulli equation is used, as mentioned above.

It is interesting to note that linear theory gives a much better estimate of the *difference* between the upper and lower surface pressures, than it does of the single-surface values. As a result, the mean and fluctuating values of the lift coefficient given by Eq. (2) are approximately correct for this case.

Finally, there is a point to be made about a relatively minor aspect of the lift behavior shown in Fig. 4. The hysteresis in $C_L$ versus $\alpha$ is slightly different from that predicted by linear theory. This small difference, also evident in the results on the other profiles, might be ascribed to the effect of airfoil thickness, but it is also the trend predicted for wall interference effects.[9] Computations or analyses of all of the cases in this paper should include the solid wind tunnel walls as outer boundaries, rather than free-air conditions.

### Case 2: NLR-7301, $\alpha = 5° + 5° \sin \omega t$

Differing from Case 1 only in airfoil geometry, Case 2 produced the data plotted in Fig. 6. The effects of both thickness and camber are apparent in the mean pressure distribution, as would be expected. However, the fluctuating pressures appear to be much less sensitive to the large aft camber and are mainly affected by the blunt leading-edge geometry. The leading-edge radius is about twice that of the 0012 airfoil, and, consequently, the peak values of $C_{p_1}$ near the leading edge are less on the NLR-7301 airfoil. It should be noted that linear theory for this case is identical to that for Case 1.

### Case 3: NACA 0012, $\alpha = 8° + 5° \sin \omega t$

Figure 7 shows the principal results for this more complex case. Increasing $\alpha_{max}$ has two main effects, compared with Case 1. First, the fluctuating pressures increase due to the nonlinear contributions of mean angle effects. Second, the upper surface boundary layer thickens, especially near the trailing edge. The former effect is most pronounced

for the in-phase pressure distribution near the leading edge, whereas the latter is the main reason for the change in the out-of-phase component of $C_p$. This change in quadrature pressure is also reflected in the sense of the $C_L - \alpha$ hysteresis loop (not shown), which was opposite to that of the two previous cases. Again, the linear-theory curves of $C_p/\alpha$, omitted for clarity in Fig. 7, would be identical to those shown in Fig. 5 for Case 1.

Case 4: NLR-7301, $\alpha = 10° + 5° \sin \omega t$

In Case 4, a thin layer of reversed boundary-layer flow was detected moving forward from the trailing edge to approximately midchord as $\alpha$ approached $\alpha_{max}$. The front edge of this reversed-flow layer then retreated toward the trailing edge as $\alpha$ decreased to $\alpha_o$, without ever producing large-scale separation of the boundary layer. However, the interaction with the inviscid flow produced the distortions in the fluctuating pressure distribution on the rear half of the airfoil that are evident in Fig. 8. *It should be mentioned* that these quantitative pressure data may suffer somewhat from the effects of tunnel side-wall boundary-layer contamination. Nevertheless, they give a good qualitative indication of the effects of mild trailing-edge separation on this airfoil and on the VR-7 airfoil.

## IV. Stall Onset: Mild Interaction

### General Features

This regime has a special practical significance, as discussed in Sec. II. For the purposes of mathematical modeling, the no-stall and stall-onset regimes are similar, since the viscous layers remain relatively thin. However, the challenge to prediction methods is greater, because the magnitude of the viscous-inviscid interaction increases rapidly with small increases in $\alpha_{max}$ in the stall-onset regime. Furthermore, depending on the airfoil geometry and $M_\infty$, the extent of flow separation may either increase or decrease with increasing reduced frequency, whereas viscous effects tend to be suppressed by unsteady effects below stall. As a result of these factors, the stall-onset regime is a narrow but important one that bridges the no-stall and light-stall domains.

Case 5: NASA 0012, $\alpha = 9° + 5° \sin \omega t$, $k = 0.20$

In the unsteady experiments at $M_\infty = 0.30$, a thin tongue of reversed flow akin to that of Case 4 was observed on the rear of the NACA 0012 airfoil for $13° \le \alpha_{max} \le 13.9°$. For $k \le 0.05$, this situation also existed for $\alpha_{max} = 14°$, but when the reduced frequency was increased above 0.10, unusual separation-like boundary-layer disturbances originated in the upper leading-edge region and propagated downstream. The boundary-layer instrumentation indicated neither reversed flow over the whole airfoil nor complete separation in the sense of a large-scale breakdown of the flow, but the thickening of the viscous layer was sufficient to cause significant distortions in the upper-surface pressure distributions and in the hysteresis loops of $C_L$ and $C_M$ versus $\alpha$. This is indicated by the bold curves in Fig. 9.

Figure 10 shows the harmonic components of the pressure distribution for this case. All four parts of the figure are different from those of the preceding no-stall case, $\alpha_{max} = 13°$, shown in Fig. 8, but the effects on the out-of-phase and second-harmonic components are particularly noteworthy.

Case 6: Vertol VR-7, $\alpha = 10° + 5° \sin \omega t$, $0.025 \le k \le 0.20$

In contrast to the NACA 0012 section, a well-defined thin layer of reversed viscous flow developed in the trailing-edge region in the stall-onset and light-stall regimes with the VR-7 airfoil. For Case 6, the chordwise extent of this reversed flow was strongly dependent on reduced frequency. This is illustrated in Fig. 11, which shows the loci of the point $\tau_w \simeq 0$ on the airfoil surface as a function of time for three values of k. The reversed-flow region is clearly delayed and suppressed by increasing unsteady effects.

The upper-surface pressure distributions are qualitatively similar over the experimental range of frequencies, as shown in Fig. 12. However, Fig. 13 shows that the extent of the trailing-edge separation has an important quantitative effect, and only the example at $k = 0.20$ can be considered truly representative of stall onset. For $k \le 0.10$, the results exhibit many of the characteristics of the next level in the hierarchy, light stall.

## V. Light Stall: Strong Interaction

### General Features

This regime for oscillating airfoils shares some of the general features of classical static stall, such as a loss of lift and significant increases in drag and nose-down pitching moment compared with the theoretical inviscid values, when $\alpha$ exceeds a certain value. In addition, the unsteady stall behavior is characterized by large phase lags and hystereses in the separation and reattachment of the viscous flow and, consequently, in the airloads. Also, the aerodynamic damping in pitch, given by $-C_M d\alpha$, can become negative, that is, unstable; this tendency is strongest in the light-stall domain.

Another *distinguishing feature* of this regime is the scale of the interaction. The vertical extent of the viscous zone tends to remain on the order of the airfoil thickness, generally less than for static stall. Consequently, this class of *oscillating airfoil problems* should be within the scope of zonal methods or thin-layer Navier-Stokes calculations with relatively straightforward turbulence modeling.

The qualitative behavior of light stall is known to be especially sensitive to airfoil geometry, reduced frequency, maximum incidence, and Mach number; also, three-dimensional effects and the type of motion are probably important. The quantitative behavior is closely related to the boundary-layer separation characteristics (for example, leading-edge versus trailing-edge separation), and to the changes in this separation behavior with $\alpha_{max}$, k, and $M_\infty$. Therefore, the possible test cases are numerous and varied. For the sake of simplicity, however, this section will concentrate on the effects of reduced frequency on two airfoils: one airfoil with trailing-edge separation characteristics and one with leading-edge separation behavior.

The former is represented by Case 6, discussed earlier and presented in Figs. 11-13. The important point here is the suppression of the amount of trailing-edge separation, and hence the magnitude of the viscous-inviscid interaction, with increasing frequency. As a result of this unsteady effect, Case 6 passes from light-stall behavior for $k \leq 0.10$ to stall-onset conditions for $k \geq 0.15$.

Case 7: NACA 0012, $\alpha = 10° + 5° \sin \omega t$, $0.025 \leq k \leq 0.20$

For $M_\infty \leq 0.2$, the light-stall behavior of the 0012 airfoil followed the trends of Case 6; that is, separation was suppressed as $k$ increased. However, at $M_\infty = 0.30$ the severity of the stall increased with increasing $k$, as the mild trailing-edge separation at low frequency gave way to the separation-like leading-edge disturbances that were noted for Case 5 for $k \geq 0.15$.

The attendant changes in the lift and pitching moment behavior are shown in Fig. 14, which provides a striking contrast to the VR-7 data in Fig. 13. The upper-surface pressure disturbances are given in Fig. 15. For $k = 0.025$, the curves generally resemble those of Fig. 12, but the results at $k = 0.20$ are an exaggeration of those shown in Fig. 9.

The maximum lift rose monotonically with $k$ for both the 0012 and VR-7 airfoils, as shown in Fig. 16. However, the figure shows that the trends of $C_{M_{min}}$ are quite different for $k > 0.10$, as the stall became more severe for the 0012 section. In fact, the behavior of $C_M$ versus $\alpha$ at $k = 0.20$ and the near-collapse of the leading-edge suction, Fig. 15b, are characteristics that approach those of deep dynamic stall, which is the next level in the hierarchy.

## VI. Deep Dynamic Stall: Viscous Dominated

### General Features

The time-dependent stall behavior in this regime is characterized by the shedding of a large vortex-like disturbance from the leading-edge region and the passage of this vortex over the upper surface of the airfoil.[1,5-7] This produces values of $C_L$, $C_M$, and $C_p$ that are far in excess of their static counterparts when $\alpha$ is increasing, and large amounts of hysteresis occur during the rest of the cycle. The scale of the interaction zone is also large; the thickness of the viscous layer is of the order of the airfoil chord during the vortex-shedding process. This poses potential problems in grid generation, spatial resolution, and turbulence modeling for numerical analyses.

This qualitative picture appears to hold over a wide range of unsteady flow conditions, airfoil geometries, Reynolds numbers, and Mach numbers, provided strong shock waves do not develop.[1,7] The quantitative behavior of the flow depends primarily on the time history of the angle of attack for the portion of the cycle when $\alpha$ exceeds the static stall angle, $\alpha_{ss}$. This feature and other details of the flow behavior will become evident in the following examples.

Case 8: NACA 0012, $\alpha = 10° + 10° \sin \omega t$, $k = 0.10$

The right-hand section of Fig. 2 shows one of the examples of deep dynamic stall for the NACA 0012 airfoil. The contrast with the static behavior and with the other unsteady stall regimes is readily apparent.

Figure 17 shows the unsteady pressure distribution on the upper surface for this case. In particular, the vortex-shedding phenomenon manifests itself in the curves at $\alpha = 16.2°$, $18.2°$, and $19.4°$; and the leading-edge suction collapses abruptly over this interval. The boundary layer separated initially from the leading-edge region at this frequency, starting at $\alpha \simeq 16°$, or $\omega t \simeq 40°$. This represented a change from abrupt trailing-edge stall[1] at $k \leq 0.05$.

Case 9: NACA 0012, $\alpha = 15° + 5° \sin \omega t$, $0.005 \leq k \leq 0.20$

One particular reduced frequency of this set of data, $k = 0.15$, produced results almost identical to those of Case 8 over the portion of the cycle for which $\alpha \geq \alpha_{ss}$. Figure 18 shows the time histories of $\alpha$, $C_L$, and $C_M$ and the corresponding hysteresis loops of $C_L$ and $C_M$ *versus* $\alpha$ superimposed on those of Case 8. The agreement between these cases is remarkable; but it should be emphasized that the results match this well only when the time histories of $\alpha$ agree.[1]

Figure 19 shows the growth of $C_{l_{max}}$ and $C_{l_{min}}$ with reduced frequency for the NACA 0012, along with the Vertol VR-7 results of the following case. The extreme values of $C_{M_{min}}$ are particularly noteworthy, as they are considerably larger than the light-stall results shown in Fig. 16.

Case 10: Vertol VR-7, $\alpha = 15° + 5° \sin \omega t$, $0.025 \leq k \leq 0.20$

At lower Mach numbers, the VR-7 airfoil exhibited trailing-edge separation behavior throughout the light-stall and deep-stall regimes.[1] However, at $M_\infty = 0.30$ an interesting change occurred in the boundary-layer characteristics from trailing-edge separation to a mixed leading- and trailing-edge stall, as the vortex shedding phenomenon increased in intensity with increasing $k$. The lift and moment data for this case are shown in Fig. 20 and the boundary-layer results are shown in Fig. 21.

The effects of vortex shedding first appeared at $k \simeq 0.05$, with a weak vortex originating around midchord. The flow reversal that preceded this vortex formation progressed slowly upstream from the trailing edge, as indicated in Fig. 21. However, a conversion to leading-edge stall began for $k \geq 0.15$ with a much stronger vortex originating at $x \simeq 0.02$. It is the distortions in the chordwise pressure distribution due to this transient vortex that produce the large values of the pitching moment that are indicated in Figs. 19 and 20.

## VII. Concluding Remarks

The 10 cases described in the previous sections illustrate most, although by no means all, of the

panorama of viscous-inviscid interactions that occur on oscillating airfoils in subsonic flow. The specific flow conditions for each case were carefully selected to emphasize the predominant characteristics of each of the four flow regimes, while minimizing the effect of the experimental uncertainties in the appropriate data. In other words, the experimental results were presented more on the basis of documenting specific trends or features of each flow, rather than on the importance of the absolute values of the measurements. Nevertheless, the data are thought to be of sufficiently high quality that including the small effects of the wind-tunnel walls would be warranted in any analysis of the test cases.

To the authors' knowledge, few of the specific cases, or their equivalents, discussed in this paper have yet been calculated. However, the unstalled cases of Sec. III would appear to be well suited to straightforward extensions of present-day zonal modeling methods for steady flows, as exemplified by the recent collection of papers in Ref. 10. Such methods should also be capable of treating the stall-onset cases of Sec. IV, although the details of the unsteady flow regions with flow reversal at the bottom of the boundary layer will surely require special treatment. The thin-layer, Reynolds-averaged Navier-Stokes methods (e.g., Ref. 11) are also appropriate for this regime, as well as for the light-stall regime. The extent to which the zonal methods can be applied to the light-stall cases is an open question. However, both approaches offer attractive alternative to the empirical correlation methods that are currently used for engineering predictions.[6,7] For this reason, coupled with its practical importance, the light-stall regime is probably the one that most warrants concentrated research efforts.

The greatest challenge to theoretical or numerical analysis is clearly the deep-stall regime. As mentioned in Sec. VI, the viscous region is very large, and it is a dominant feature of the flow field, so that thin-layer approximations and turbulence models based on boundary-layer length scales are probably suspect. New approximate or semiempirical methods that take advantage of the predominance of the vortex-shedding phenomena might be feasible, in addition to the discrete-vortex methods[6,7] that are sometimes applied to bluff-body flows, provided they are not limited by the assumptions that have to be made to start the calculations. The long-range need seems to be for Navier-Stokes calculations with improved turbulence modeling.

In conclusion, the experimental results described in this paper provide well-defined conditions and data that can be used to evaluate existing theoretical and numerical prediction methods. The information presented should also help future investigators decide on the approach that is the most appropriate for the particular domains of interest to them.

## References


[1]McCroskey, W. J., McAlister, K. W., Carr, L. W., Pucci, S. L., Lambert, O., and Indergand, R. F., "Dynamic Stall on Advanced Airfoil Sections," American Helicopter Society Preprint 80-1, May 1980.

[2]McCroskey, W. J., McAlister, K. W., Pucci, S. L., Carr, L. W., Lambert, O., and Indergand, R. F., "An Experimental Study of Dynamic Stall on Advanced Airfoil Sections," NASA TM in preparation, 1981.

[3]Davis, S. S. and Malcolm, G. N., "Unsteady Aerodynamics of Conventional and Supercritical Airfoils," AIAA Paper 80-0734, Seattle, Wash., Apr. 1980.

[4]Dowell, E. H., Williams, M. H., and Chi, M. R., "An Assessment of Theoretical Models for Viscous and Transonic Flow," Paper No. 1, AGARD Specialists' Meeting on Boundary Layer Effects on Unsteady Airloads, Aix-en-Provence, France, Sept. 1980.

[5]Young, W. H., Jr., "Fluid Mechanics Mechanisms in the Stall Process of Airfoils for Helicopters," Symposium on Numerical and Physical Aspects of Aerodynamic Flows, Long Beach, Calif., Jan. 1981.

[6]Beddoes, T. S., "A Qualitative Discussion of Dynamic Stall," and "Prediction Methods for Unsteady Separated Flows," Papers No. 3 and 15, Special Course on Unsteady Aerodynamics, AGARD Report R-679, June 1980.

[7]McCroskey, W. J., "Some Unsteady Separation Problems for Slender Bodies," and "Prediction of Unsteady Separated Flows on Oscillating Airfoils," Papers No. 8 and 12, Three Dimensional and Unsteady Separation at High Reynolds, AGARD Lecture Series LS-94, Feb. 1978.

[8]Bisplinghoff, R. L., Ashley, H., and Halfman, R. L., Aeroelasticity, Addison-Wesley, Reading, Mass., 1957.

[9]Fromme, J. A., Golberg, M. A., and Werth, J., "Unsteady Two-Dimensional Airloads Acting on Oscillating Thin Airfoils in Subsonic Ventilated Wind Tunnels," NASA CR-2967, 1978.

[10]Monnerie, B. and Quinn, B., eds., "Computation of Viscous-Inviscid Interactions," AGARD Conference Proceedings CP-291, Oct. 1980.

[11]Baldwin, B. S. and Lomax, H., "Thin Layer Approximation and Algebraic Model for Separated Turbulent Flows," AIAA Paper 78-257, Huntsville, Ala., Jan. 1978.

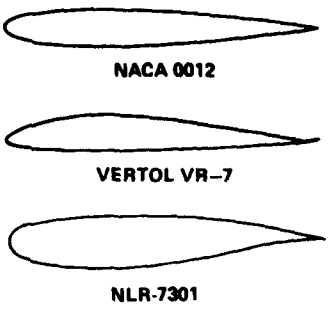


Fig. 1 Airfoil cross sections.

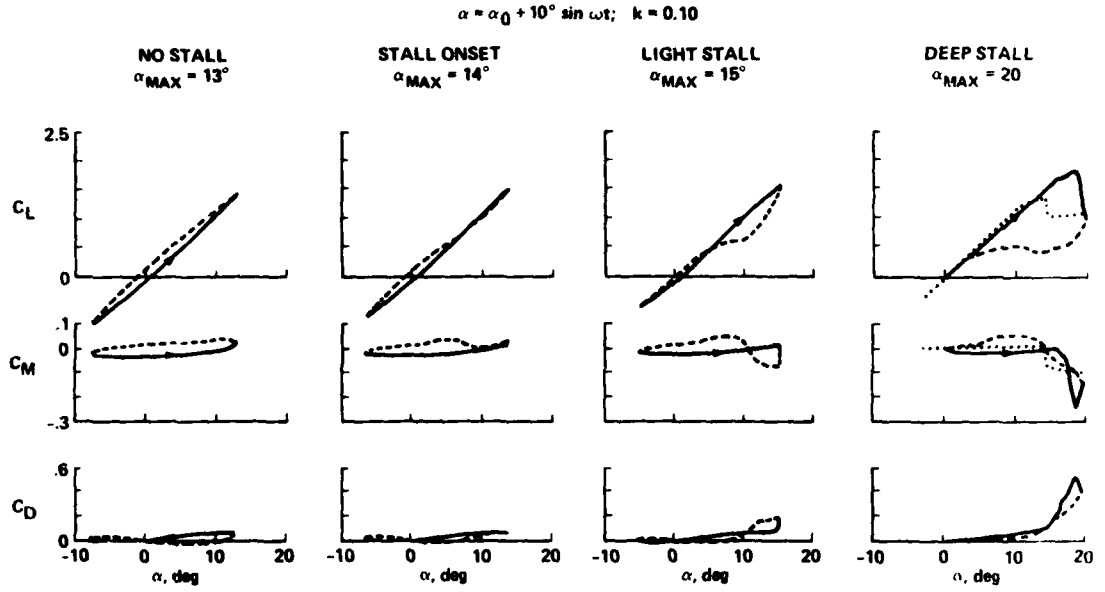


Fig. 2 Four regimes of unsteady airloads on the NACA 0012 airfoil; solid lines denote increasing angle of attack, dashed lines decreasing α, dotted lines static data.

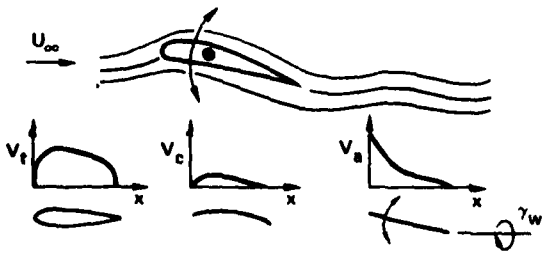


STEADY: $U = V_t + V_c + V_a \alpha$

UNSTEADY: $U = V_t + V_c + V_a \alpha_0 + V_a \alpha_1 f(x,t)$

$$C_p = 1 - U^2 - \frac{\partial \phi}{\partial t} + \mathcal{O}(M_\infty^4)$$

Fig. 3 Sketch of the flow due to thickness, camber, and angle of attack on an oscillating airfoil.

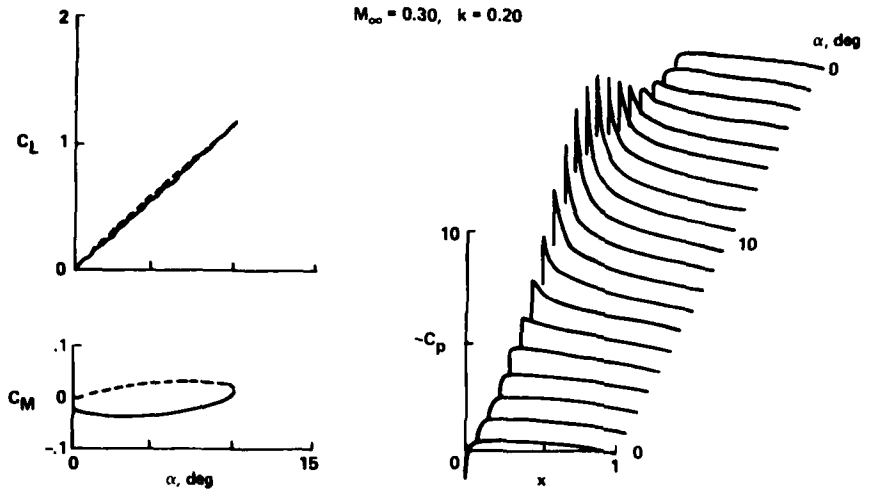


Fig. 4 Unsteady pressures and airloads for Case 1; NACA 0012 airfoil, $\alpha = 5° + 5° \sin \omega t$, k = 0.20.

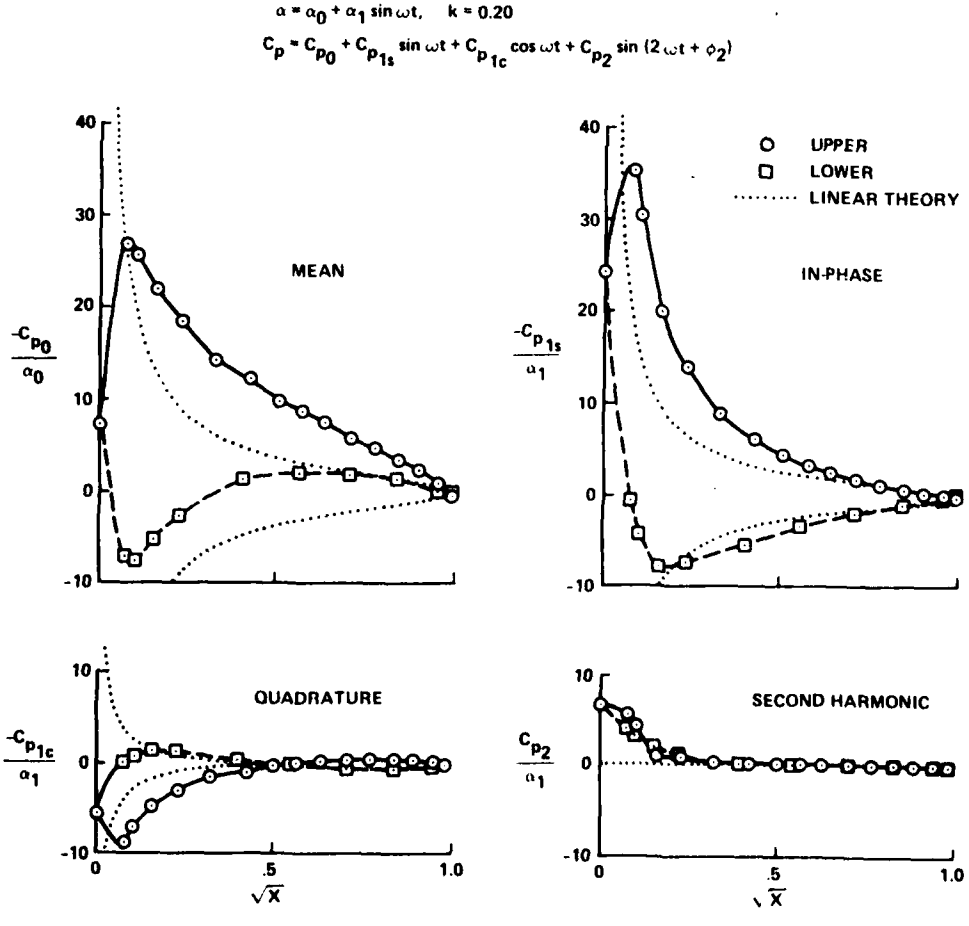


Fig. 5 Harmonic components of unsteady pressures for Case 1; NACA 0012 airfoil, $\alpha = 5° + 5° \sin \omega t$.

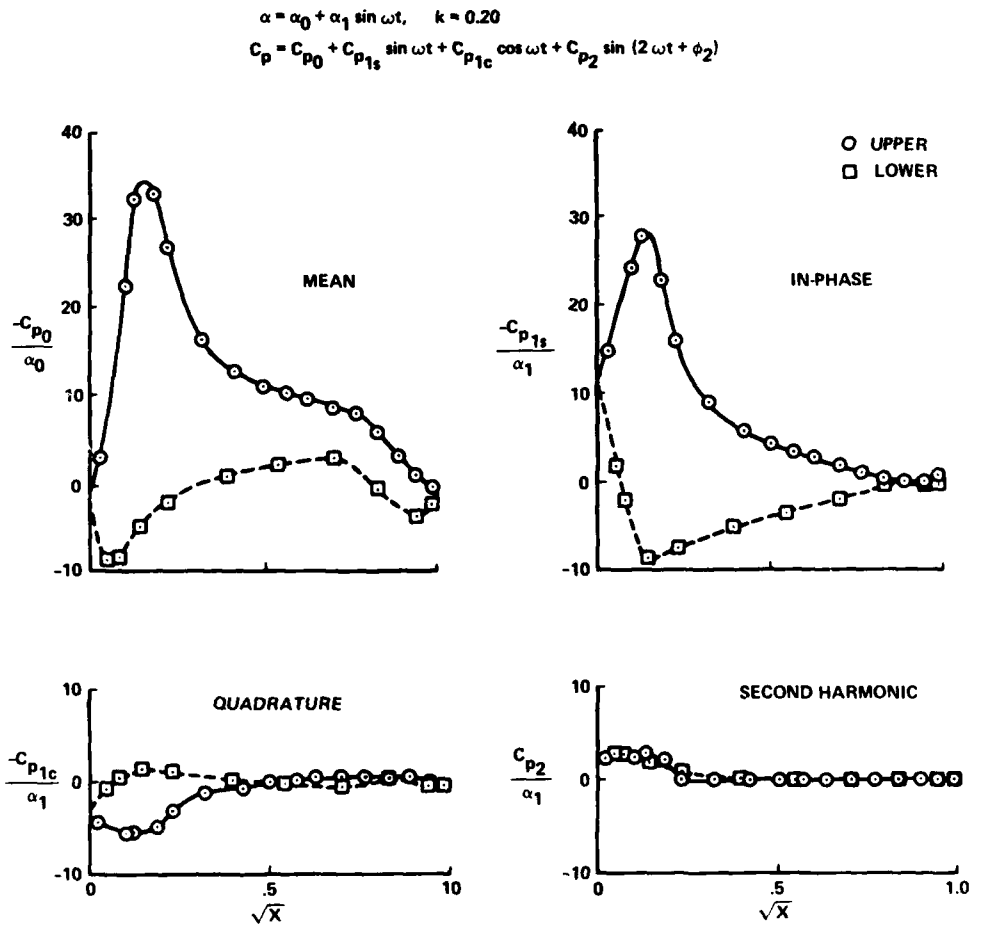


Fig. 6 Harmonic components of unsteady pressures for Case 2; NLR-7301 airfoil, $\alpha = 5° + 5° \sin \omega t$.

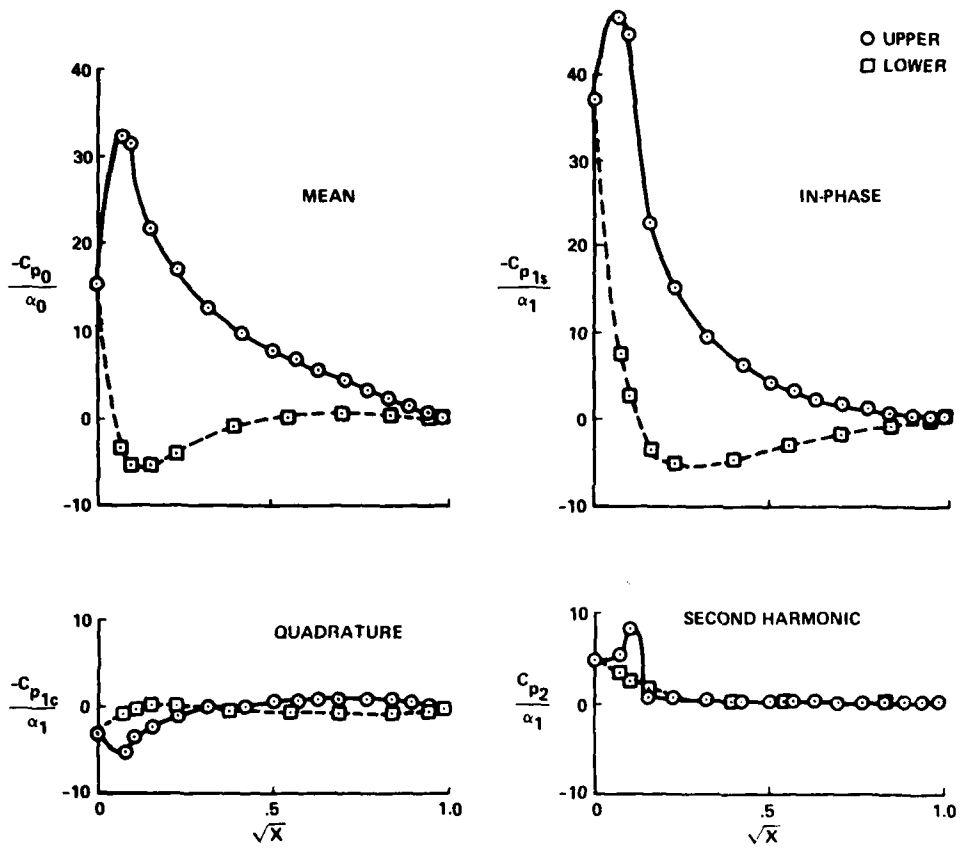


Fig. 7 Harmonic components of unsteady pressures for Case 3; NACA 0012 airfoil, $\alpha = 8° + 5° \sin \omega t$.

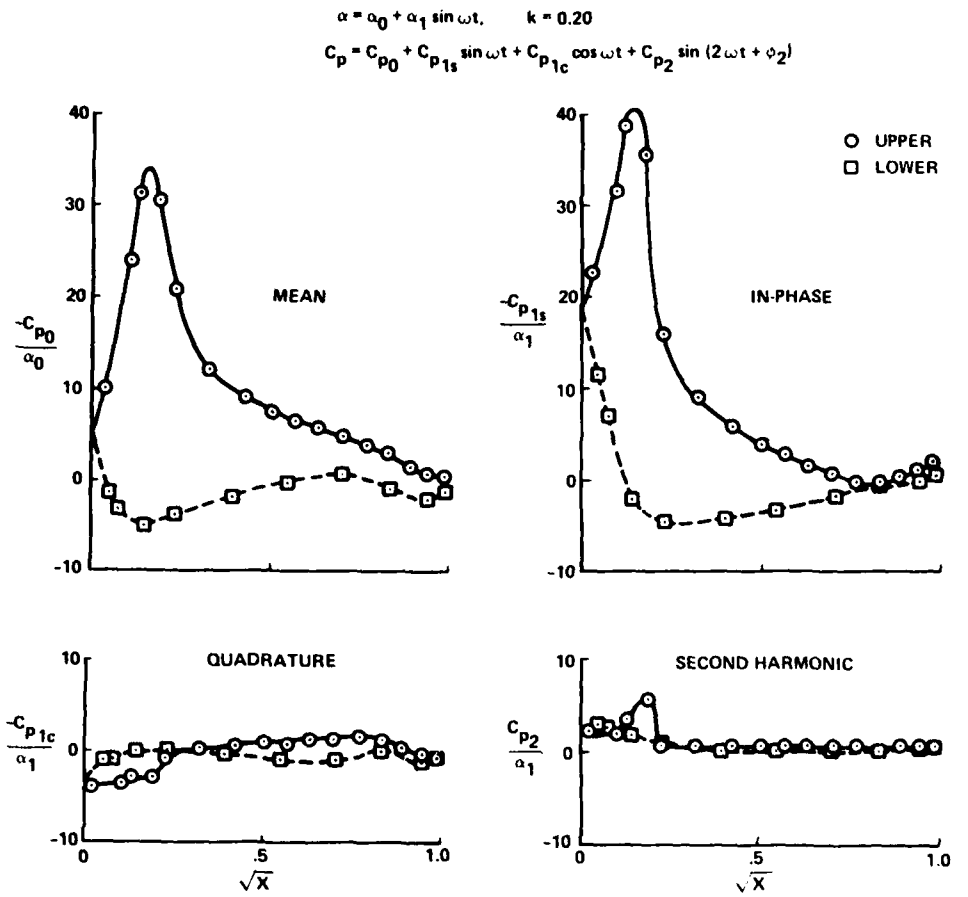


Fig. 8 Harmonic components of unsteady pressures for Case 4; NLR-7301 airfoil, $\alpha = 10° + 5° \sin \omega t$.

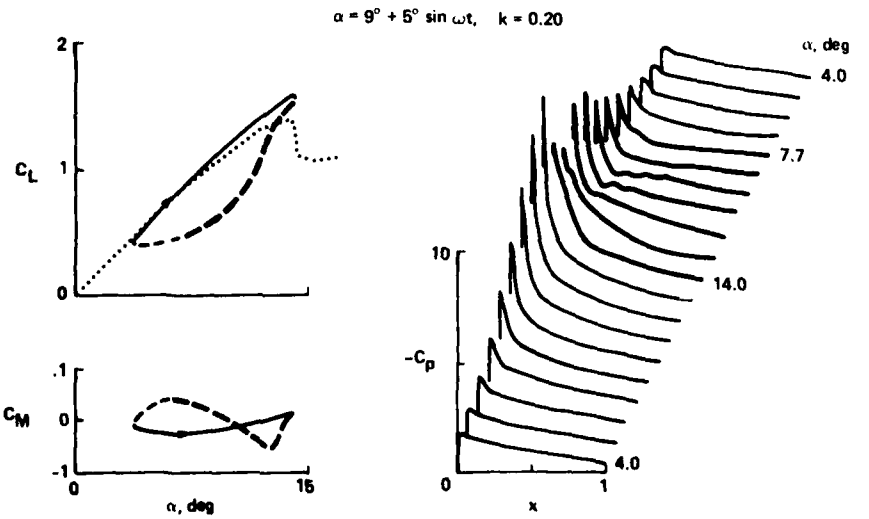


Fig. 9 Unsteady pressures and airloads for Case 5.

$\alpha = \alpha_0 + \alpha_1 \sin \omega t, \quad k = 0.20$

$C_p = C_{p_0} + C_{p_{1s}} \sin \omega t + C_{p_{1c}} \cos \omega t + C_{p_2} \sin (2\omega t + \phi_2)$

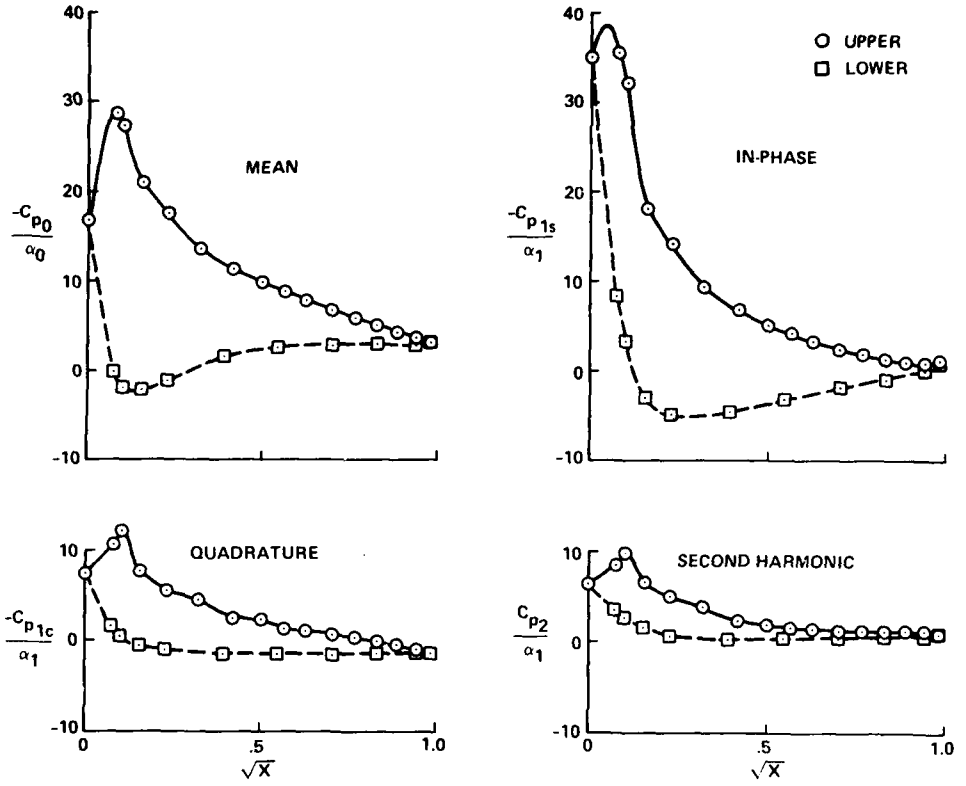


Fig. 10 Harmonic components of unsteady pressures for Case 5; NACA 0012 airfoil, $\alpha = 9° + 5° \sin \omega t$.

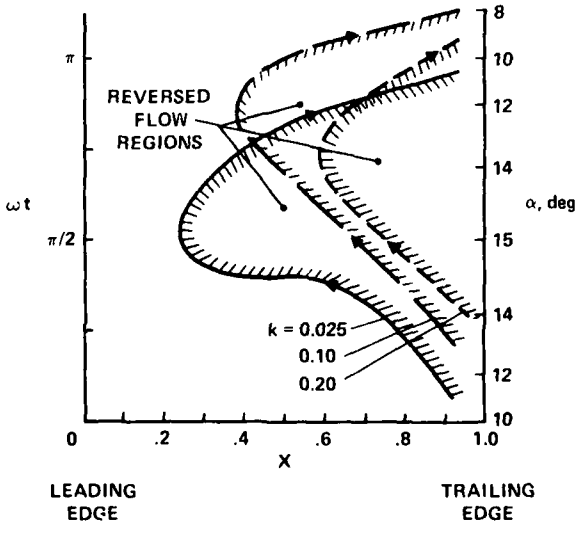


Fig. 11 Reversed flow boundaries on the VR-7 airfoil, Case 6; $\alpha = 10° + 5° \sin \omega t$.

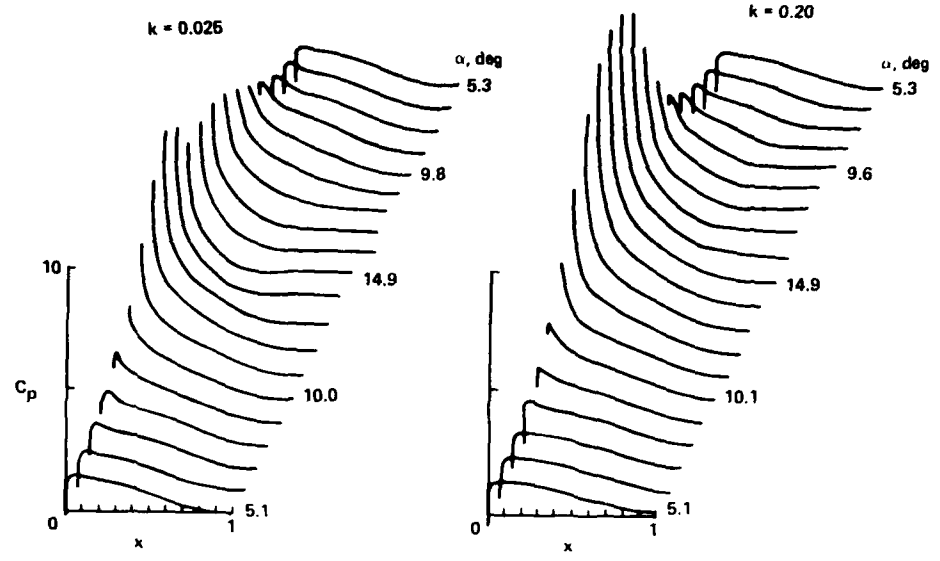


Fig. 12 Unsteady pressures for Case 6; VR-7 airfoil, $\alpha = 10° + 5° \sin \omega t$.

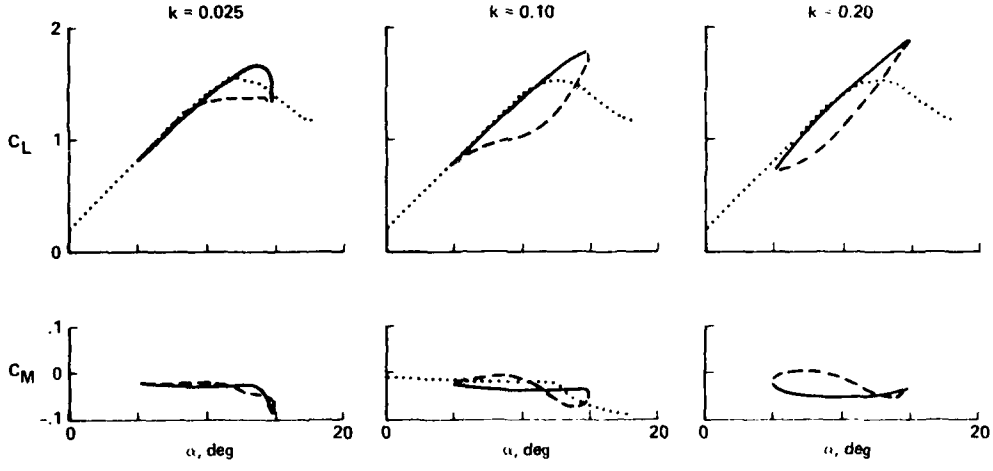


Fig. 13 Unsteady airloads for Case 6; VR-7 airfoil, $\alpha = 10° + 5° \sin \omega t$.

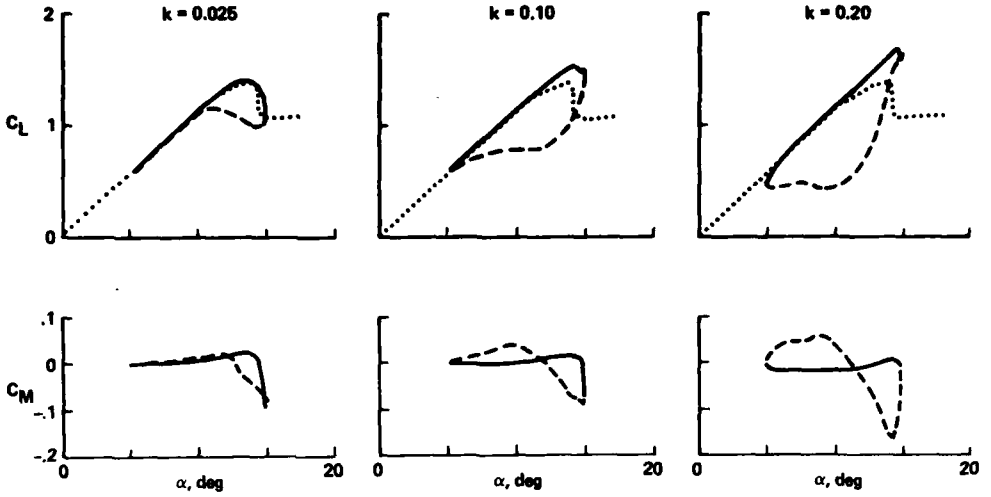


Fig. 14 Unsteady airloads for Case 7; NACA 0012 airfoil, $\alpha = 10° + 5° \sin \omega t$.

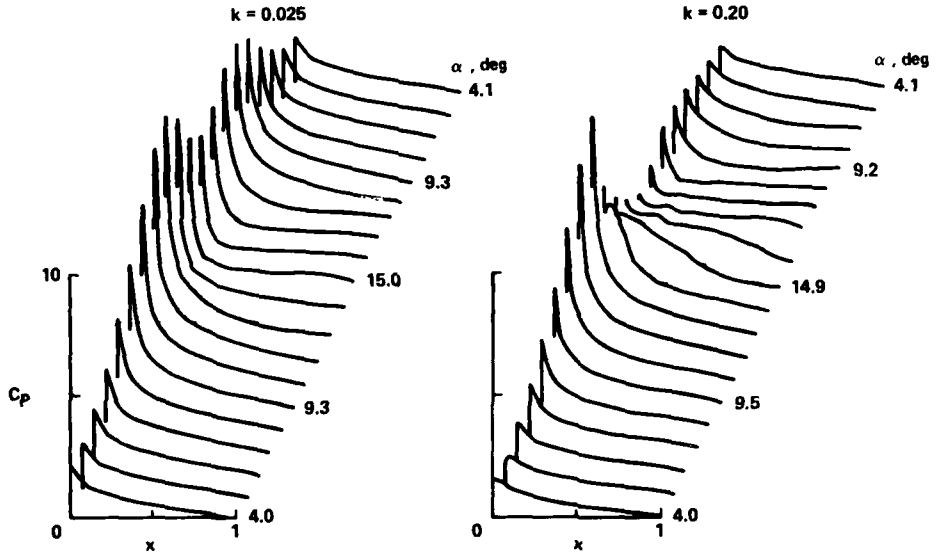


Fig. 15 Unsteady pressures for Case 7; NACA 0012 airfoil, $\alpha = 10° + 5° \sin \omega t$.

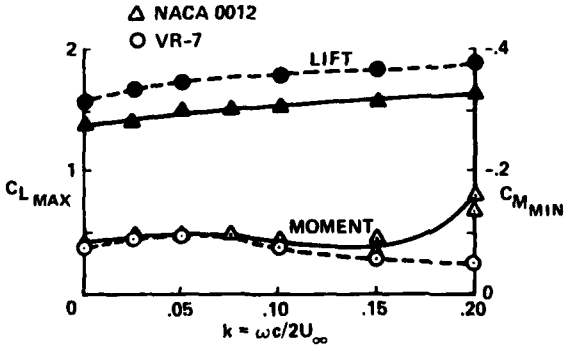


Fig. 16 Maximum lift and moment values on the NACA 0012 and VR-7 airfoils for $\alpha = 10° + 5° \sin \omega t$.

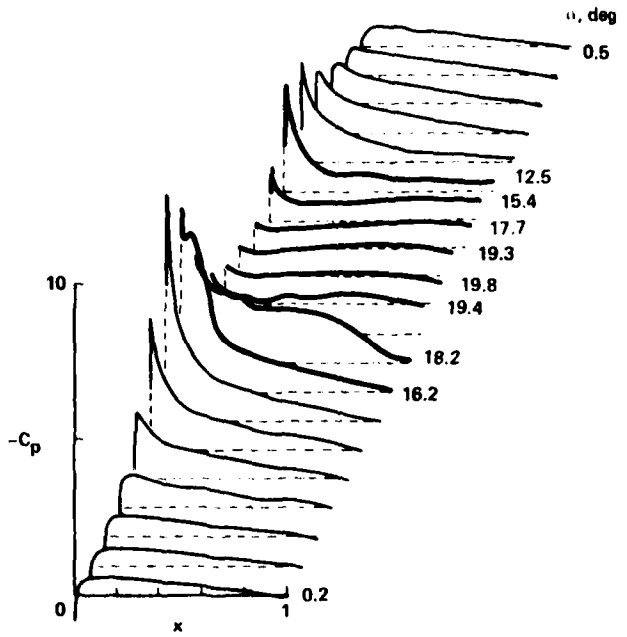


Fig. 17 Unsteady pressures for Case 8; NACA 0012 airfoil, $\alpha = 10° + 10° \sin \omega t$, $k = 0.10$.

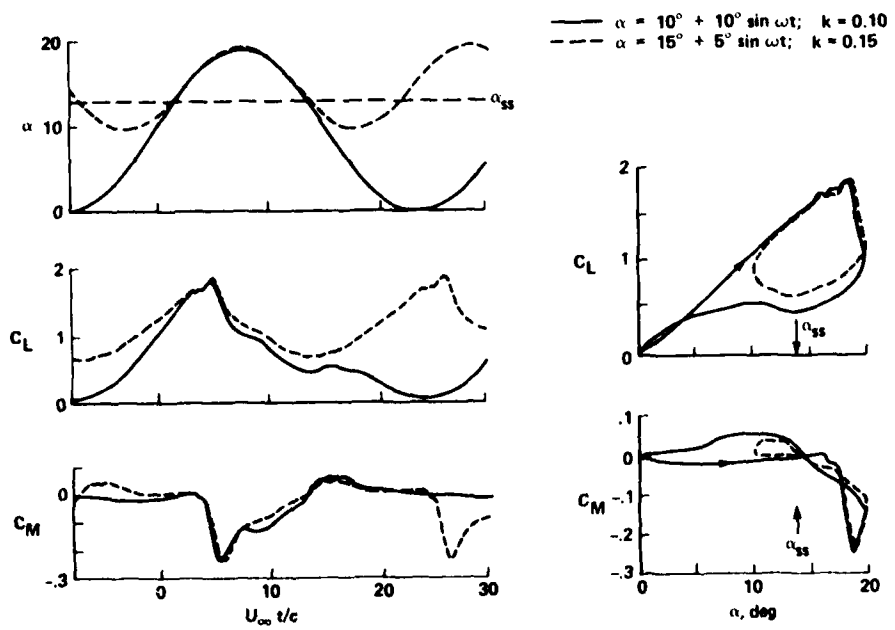


Fig. 18 Unsteady airloads on the NACA 0012 airfoil, Cases 8 and 9.

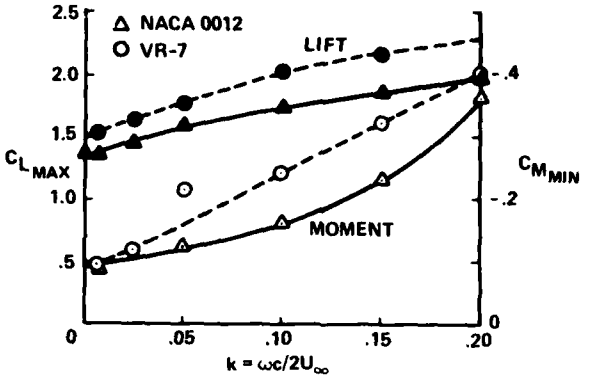


Fig. 19 Maximum lift and moment values on the NACA 0012 and VR-7 airfoils for $\alpha = 15° + 5° \sin \omega t$.

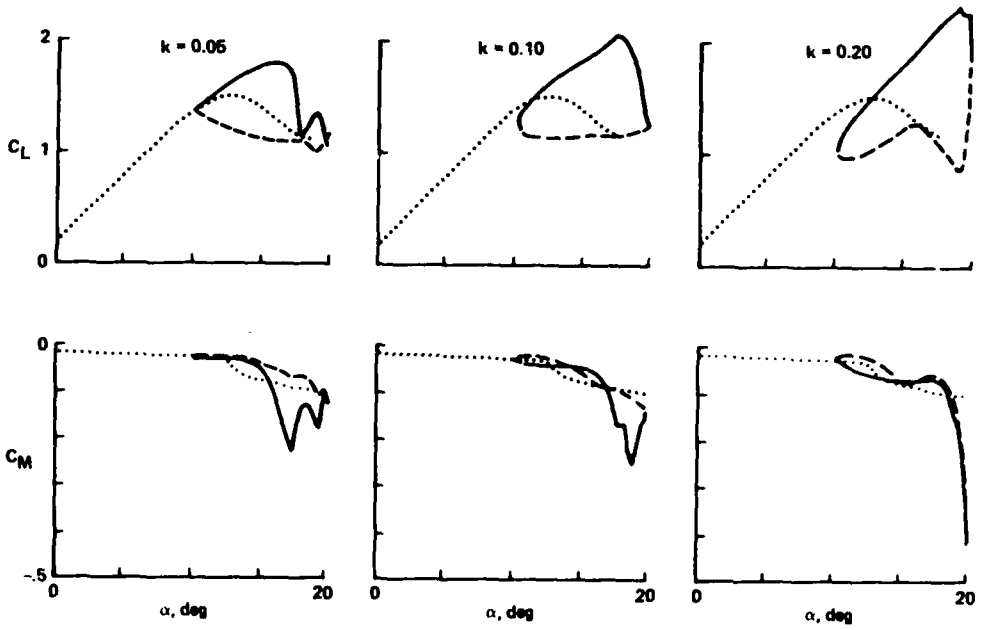


Fig. 20 Unsteady airloads for Case 10; VR-7 airfoil, $\alpha = 15° + 5° \sin \omega t$.

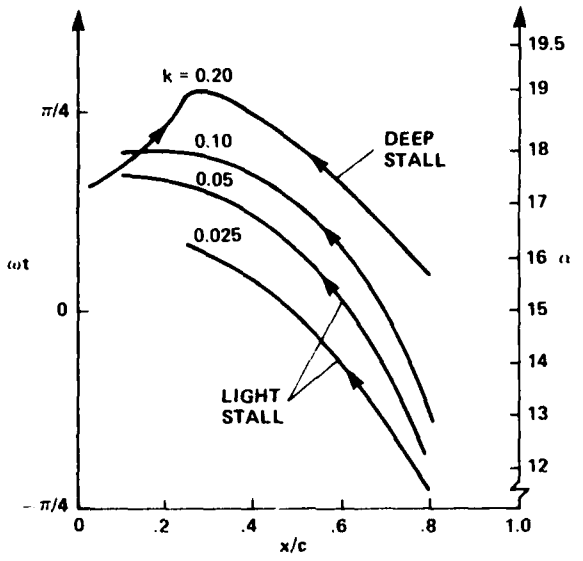


Fig. 21 Loci of boundary-layer flow reversal on the VR-7 airfoil, Case 10; $\alpha = 15° + 5° \sin \omega t$.


DAT
ILM